Monsoon Depression Amplification by Horizontal Shear and Humidity Gradients: A Shallow Water Perspective

D. L. SUHAS[a] AND WILLIAM R. BOOS[a,b]

[a] *Department of Earth and Planetary Science, University of California, Berkeley, Berkeley, California*
[b] *Climate and Ecosystem Sciences Division, Lawrence Berkeley National Laboratory, Berkeley, California*

(Manuscript received 25 June 2022, in final form 25 October 2022)

ABSTRACT: Transient, synoptic-scale vortices produce a large fraction of total rainfall in most monsoon regions and are often associated with extreme precipitation. However, the mechanism of their amplification remains a topic of active research. For monsoon depressions, which are the most prominent synoptic-scale vortex in the Asian–Australian monsoon, recent work has suggested that meridional gradients in zonal wind in the vortex environment may produce growth through barotropic instability, while meridional gradients in environmental humidity have also been proposed to cause amplification through coupling with precipitating convection. Here, a two-dimensional shallow water model on a sphere with parameterized precipitation is used to examine the relative role played by these two environmental gradients. By systematically varying the meridional moisture gradient and meridional wind shear for both weak, quasi-linear waves and finite-amplitude isolated vortices, we show that rotational winds in the initial vortex are amplified most strongly by meridional shear of the environmental zonal wind, while vortex precipitation rates are most sensitive to environmental moisture gradients. The growth rate in the presence of both gradients is less than the sum of growth rates in the presence of isolated gradients, as the phase relation between moisture and vorticity anomalies becomes distorted with increasing shear. These results suggest that background meridional gradients in both zonal wind and environmental humidity can contribute to the amplification of vortices to monsoon depression strength, but with some degree of decoupling of the dry rotational flow and the moist convection.

KEYWORDS: Instability; Shallow-water equations; Diabatic heating; Intensification; Monsoons; Synoptic-scale processes

1. Introduction

Synoptic-scale low pressure systems are often observed in the vast South Asian and Australian monsoon regions, as well as in the east Pacific where the intertropical convergence zone (ITCZ) is positioned roughly 1000 km north of the equator (Hurley and Boos 2015). These vortices account for a large fraction of seasonal mean rainfall in monsoon regions (Godbole 1977; Hunt and Fletcher 2019; Hurley and Boos 2015). In the Asian–Australian region, the more intense instances of these systems are known as monsoon depressions, and are often associated with extreme rainfall (Ajayamohan et al. 2010; Fletcher et al. 2018). Many attempts have been made to understand the mechanisms governing the evolution of monsoon depressions and, more generally, monsoon low pressure systems, invoking hydrodynamic instabilities that amplify the vortex at the expense of the background winds (Mishra and Salvekar 1980; Saha and Chang 1983; Diaz and Boos 2019a,b) or through its coupling with moist convection (Krishnamurti et al. 1976; Adames and Ming 2018a; Diaz and Boos 2021a). However, the exact mechanism through which these weak disturbances intensify into monsoon depressions remains a topic of active research (Clark et al. 2020; Diaz and Boos 2021a,b).

A strong easterly vertical wind shear characterizes the region in which monsoon depressions form leading many studies to invoke some form of baroclinic instability to explain the growth of monsoon depressions (Mishra and Salvekar 1980; Saha and Chang 1983). These theories often require the coupling of baroclinic instability with the condensation and precipitation of water (Moorthi and Arakawa 1985; Salvekar et al. 1986; Krishnakumar et al. 1992). However, a key feature of all forms of baroclinic instability is the upshear tilt of potential vorticity anomalies against the vertical gradient in background zonal wind (Cohen and Boos 2016); this contrasts with the upright or slight downshear tilt of potential vorticity in observed monsoon depressions (Keshavamurty 1972; Cohen and Boos 2016). These results suggest that baroclinic instability is not the primary mechanism for the growth of monsoon depressions.

Along with strong vertical wind shear, the South Asian monsoon also exhibits strong meridional shear of the zonal wind (Fig. 1b). A weaker but qualitatively similar wind shear is also observed over the east Pacific (not shown), which is another region where synoptic-scale tropical vortices grow. This meridional shear of zonal wind, hereafter referred to simply as horizontal shear, raises the possibility that the monsoon basic state may be barotropically unstable, with monsoon depressions growing at the expense of the background horizontal shear. Early evidence for barotropic growth of monsoon depressions was mixed (Subrahmanyam et al. 1981; Nitta and Masuda 1981; Goswami et al. 1980; Lindzen et al. 1983; Shukla 1977; Krishnakumar et al. 1992; Rajamani and Sikdar 1989; Krishnamurti et al. 2013), although some studies arguing against barotropic instability

Corresponding author: D. L. Suhas, suhasdl@berkeley.edu

DOI: 10.1175/JAS-D-22-0146.1

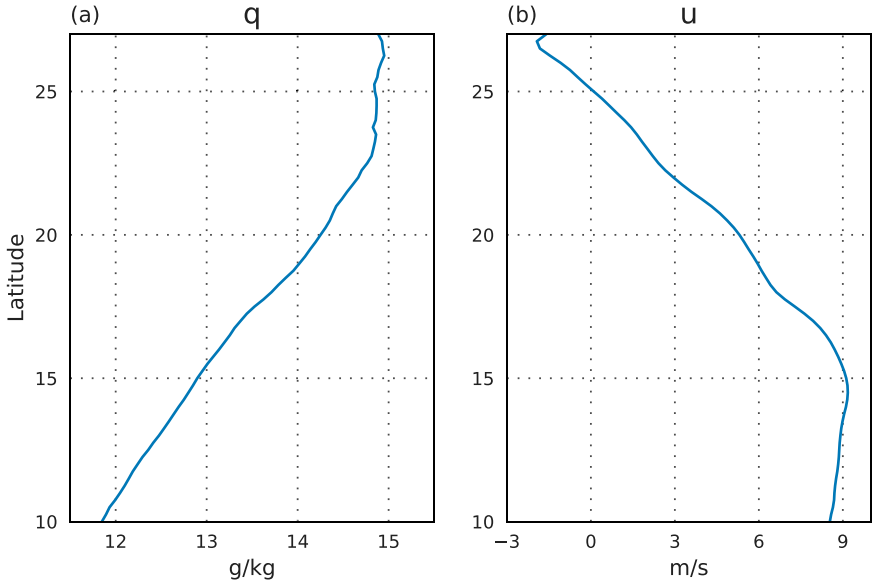

FIG. 1. The zonal mean of the JJAS basic-state (a) specific humidity and (b) zonal wind at 850 hPa over the South Asian region. The mean states are obtained by averaging the ERA5 data over the longitudes 80°–90°E and for the years 1979–2020. The plots are limited to 27°N, as the region northward of it is below the terrain surface. The region exhibits a moisture gradient, which increases with latitude and a meridional wind shear, centered roughly around 20°N.

as a relevant mechanism used basic states that differed substantially from observations or focused on upper-tropospheric rather than lower-tropospheric modes; for a discussion see the last section of Diaz and Boos (2019a). Recent studies using three-dimensional basic states drawn from modern reanalyses have shown that barotropic growth can explain the structure and propagation of observed monsoon depressions (Diaz and Boos 2019a,b). Barotropic conversion from the background meridional shear has also been shown to contribute to the energy of east Pacific easterly waves (Rydbeck and Maloney 2014). Nevertheless, even if barotropic growth is important, moist convection and diabatic heating likely play an essential role in achieving positive net growth rates in observed monsoon depressions, especially with frictional dissipation and a zonally asymmetric basic state (Krishnamurti et al. 1976; Adames and Ming 2018a; Diaz and Boos 2021a).

An alternate route for the growth of monsoon depressions was proposed by Adames and Ming (2018a). Using a linear model, they showed the growth of a synoptic-scale monsoon disturbance can occur due to interactions between meridional moisture advection, moist convection, and potential vorticity. This mechanism, termed moisture–vortex instability, favors growth in regions where the background specific humidity increases poleward, such as in South Asia (Fig. 1a) and the east Pacific, and can operate even in the absence of barotropic or baroclinic instability. A similar instability was obtained by Sobel et al. (2001) in the limit of a weak temperature gradient balance. Adames (2021) further explored this mechanism in a linear two-layer quasigeostrophic model, generalizing it to show that in the presence of a poleward MSE gradient (which might even exist due to a temperature gradient in the absence of moisture gradient), the instability grows at the expense of any baroclinic instability that may exist in monsoon regions. However, both Adames and Ming (2018a) and Adames (2021) used linear quasigeostrophic models without background horizontal shear, which may not be relevant to observed monsoon depressions given their moderate Rossby numbers and the strongly sheared zonal winds in which they are embedded (Boos et al. 2015).

Here we use a fully nonlinear model to examine the evolution of disturbances in a basic state with both strong meridional moisture gradients and strong zonal flow. Specifically, we examine the growth of monsoon depression–like vortices using a two-dimensional shallow water model with parameterized moist convection. As recent studies have suggested that baroclinic instability is inconsistent with the growth of observed monsoon depressions (Cohen and Boos 2016), we mainly consider the roles played by barotropic instability and moisture–vortex instability. This work is complementary to the simulations conducted with more complex cloud-system-resolving models (Diaz and Boos 2019b) and global climate models (Adames and Ming 2018b), because it enables us to more cleanly control the separate and combined influences of gradients in humidity and wind. The model used here also allows us to simulate the nonlinear evolution of finite-amplitude vortices without linearization and the quasigeostrophic approximation.

We aim to determine how barotropic instability and moisture–vortex instability might interact when a monsoon depression–like vortex exists in a basic state with meridional gradients in both humidity and zonal wind. Are both gradients needed for growth, or is moist convection without a moisture gradient

sufficient? Do the two instability mechanisms amplify or inhibit each other? The model framework and numerical details are discussed in the next section. The growth of weak, quasi-linear sinusoidal vorticity anomalies are examined in section 3, then the evolution of strong isolated vortices is presented in section 4. Section 5 interpret some of these results and conclusions are summarized in section 6.

2. Model details

This study uses a single-layer moist shallow water model on a rotating sphere, of the form (Gill 1982; Bouchut et al. 2009; Zeitlin 2018; Suhas and Sukhatme 2020)

$$\begin{aligned} \frac{\partial \zeta}{\partial t} + \nabla \cdot (\mathbf{u}\zeta_a) &= 0, \\ \frac{\partial \delta}{\partial t} - \mathbf{k} \cdot \nabla \times (\mathbf{u}\zeta_a) &= -\nabla^2\left(\frac{\mathbf{u}\cdot\mathbf{u}}{2} + gh\right), \\ \frac{\partial h}{\partial t} + \nabla \cdot (\mathbf{u}h) &= -\chi\mathcal{P}, \\ \frac{\partial q}{\partial t} + \nabla \cdot (\mathbf{u}q) &= -\mathcal{P}\cdot \end{aligned} \tag{1}$$

The above system contains the vorticity equation, the divergence equation, the mass continuity equation, and a moisture equation, in that sequence. In these equations, $\mathbf{u} = (u, v)$ is the horizontal flow, ζ is the relative vorticity, ζ_a is the absolute vorticity, and δ is the divergence. The shallow water layer has a depth of $h(x, y, t)$, with H being the undisturbed mean of $h(x, y, t)$ (the value of which is discussed below).

The moisture equation governs the evolution of the column water vapor (q), with precipitation ($\mathcal{P}$) acting as a moisture sink. Precipitation is modeled using a Betts–Miller form (Betts 1986) dependent on the column water vapor (Muller et al. 2009), specifically $\mathcal{P} = (q - q_s)\Theta(q - q_s)/\tau_c$, where q_s is the prescribed saturation column water vapor, $\tau_c = 12$ h is the condensation time scale and Θ is the Heaviside function (Suhas and Sukhatme 2020). Moisture couples to the mass equation through precipitation, with χ acting as a conversion factor similar to the latent heat. Since we are mainly interested in the growth of anomalies over the initial few days of model time, no large-scale forcing, damping, or surface evaporation is included.

This model formulation has been used to study the development of fronts and nonlinear waves (Bouchut et al. 2009), the emergence of modons and geostrophic adjustment (Rostami and Zeitlin 2019a,b), the transient, precipitating response to tropical forcings and the influence of moisture gradients (Suhas and Sukhatme 2020), and the effects of moisture on barotropic and baroclinic instability (Lambaerts et al. 2011, 2012; Rostami and Zeitlin 2017; Bembenek et al. 2021). While some studies have shown that barotropic instability can intensify in the presence of water condensation (Lambaerts et al. 2011; Rostami and Zeitlin 2017), those studies did not examine the influence of a horizontal moisture gradient nor consider a monsoon-like basic state. Here, our aim is to examine the growth of the vortex in the presence of a moisture gradient without resorting to these restrictions.

The shallow water equations are solved using a pseudo-spectral method on a sphere using a library for spherical harmonic transforms for numerical simulations (SHTns; Schaeffer 2013). The simulations are run at a resolution of 512 (longitude) × 256 (latitude), and triangularly truncated with a maximum resolved wavenumber of 170. Time stepping uses a third-order Adams–Bashforth integrator with a time step of 30 s and a Δ^4 hyperviscosity for small-scale dissipation.

A wide range of mean heights H have been used by various studies, with values ranging from a few hundred meters to a few kilometers. While a mean height of 200–300 m corresponds to the dry phase speeds of the first baroclinic mode in the tropics (Wheeler et al. 2000; Kraucunas and Hartmann 2007), larger heights are necessary to generate the observed mean states of the zonal flows in the midlatitudes (Galewsky et al. 2004; Paldor et al. 2021). Our results are not greatly affected by this choice of H (we looked at values of H ranging from 300 m to 10 km), but to accommodate the strong meridional height gradients necessary to generate the required basic-state zonal flow, we chose a basic-state depth of 1000 m; this yields a dry Kelvin wave speed (c_d) of about 100 m s^{-1} (Kraucunas and Hartmann 2007; Monteiro et al. 2014).

The choice of moist parameters q_s and χ is somewhat arbitrary, as only the product χq influences the coupling of moisture with the dynamics. We set the maximum magnitude of q_s to 1 m, and select $\chi = 900$. This yields a moist Kelvin wave speed, $c_m \approx 0.3c_d$ (Bouchut et al. 2009; Frierson et al. 2004). The model is initialized with a state of saturation (i.e., $q = q_s$), so at initial times the gradient of prescribed saturation column water vapor sets the gradient of the moisture field. We introduce a delay in the convective onset by setting the value of the condensation time scale $\tau_c = 12$ h, which has been used in other theoretical models of the Asian monsoon (Adames and Ming 2018a).

We use two types of initial perturbations. First, we study the response to small-amplitude sinusoidal vorticity anomalies, which allows us to examine the evolution of a disturbance of a single wavenumber without strong nonlinear effects. Next, we consider a more nonlinear scenario, where the initial perturbation takes the form of a finite-amplitude, isolated vortex. Both of these types of initial perturbations are centered at 20°N, a typical latitude at which many monsoon depressions form (Sikka 1978); our conclusions are insensitive to small variations in the choice of base latitude. We explore the time evolution of these initial perturbations in the presence of a varying meridional basic-state moisture gradient q_{sy} and a varying meridional wind shear expressed as a localized basic-state vorticity maximum ζ_s; sample basic-state moisture and wind profiles are shown in Fig. 2. The strength of the horizontal wind shear is controlled by varying the magnitude of an imposed vorticity strip, following Diaz and Boos (2021a). For simplicity, we have centered both the basic-state moisture gradient and horizontal shear zone near 20°N, although in the observed South Asian mean state they are centered slightly away from this latitude (Fig. 1).

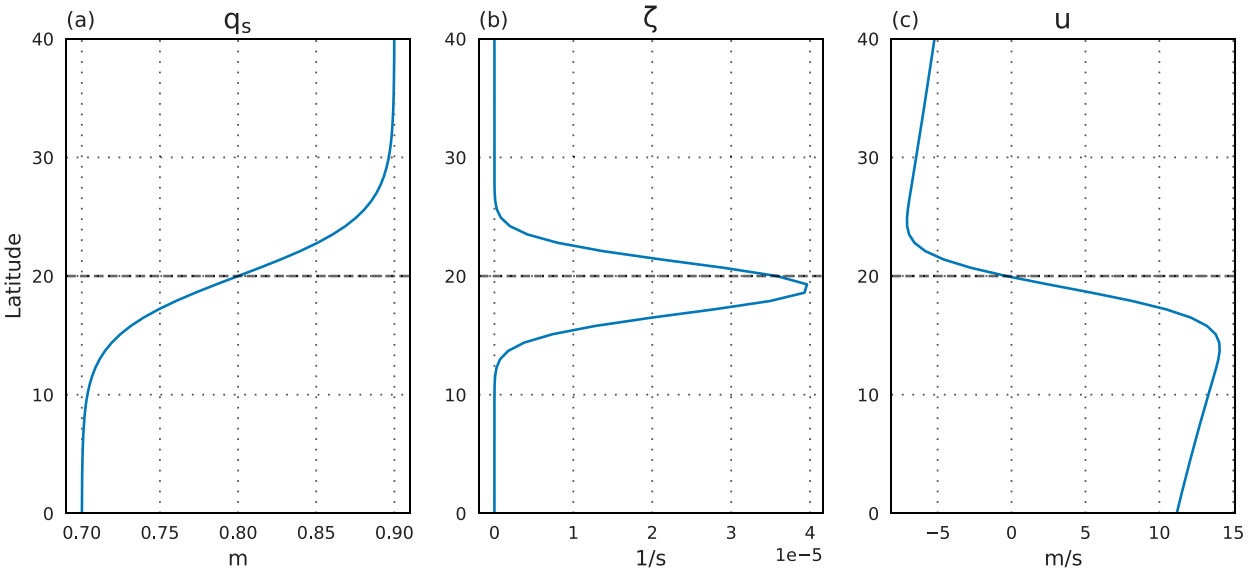

FIG. 2. Profile of the (a) imposed saturation column water vapor (q_s) and (b) Gaussian vorticity strip, which yields a (c) meridionally sheared zonal wind. Here, the basic-state saturation moisture has a gradient of $q_{sy} = 0.2$ m, and the wind shear is $\zeta_s = 4 \times 10^{-5}$ s^{-1}. All the saturation moisture profiles considered in this study have a value of 0.8 m at 20°N, and the gradient value refers to the maximum change in magnitude between the equator and the pole. Zonal wind has a zero crossing at 20°N. For convenience, we refer the wind shear with the magnitude of the corresponding vorticity strip.

3. Quasi-linear sinusoidal modes

We examine the response of our shallow water system to small-amplitude sinusoidal vorticity anomalies for a range of basic-state moisture gradients (q_{sy}) and horizontal wind shears (ζ_s). This choice of a weak initial perturbation ensures that the growth is nearly linear, at least in the initial stages. The sinusoidal vorticity anomaly is centered at $\phi_0 = 20$°N and is of the form

$$\zeta'(\lambda, \phi) = \zeta_{\text{pert}} \sin(k\lambda) \exp\left[-\left(\frac{\phi - \phi_0}{\Delta\phi}\right)^2\right], \tag{2}$$

where the perturbation magnitude $\zeta_{\text{pert}} = 1 \times 10^{-7}$ s^{-1}, $k = 15$ is the zonal wavenumber, λ is longitude, ϕ is latitude, and $\Delta\phi = 5°$. We also performed experiments with varying zonal wavenumbers and, similar to Adames and Ming (2018a), found that in the presence of a basic-state moisture gradient, the eddy energy growth was strongest around wavenumber $k = 15$. With basic-state horizontal wind shear and no moisture gradient, the fastest growth was also found in the vicinity of $k = 15$. Hence, we only present results for initial anomalies with zonal wavenumber 15.

To begin, we study the evolution of an initial sinusoidal anomaly without basic-state shear or moisture gradients, in order to confirm that at least one of these basic-state properties is needed for anomaly growth. In this set of experiments, basic-state horizontal wind shear is absent ($\zeta_s = 0$). The moist coupling parameter (χ) is set to 0 in a dry configuration, while in a moist run we impose a uniform background moist saturation field ($q_{sy} = 0$, i.e., no basic-state moisture gradient). The main objective here is to see whether an anomaly can grow in the absence of both basic-state gradients, and how the inclusion of moisture modifies the dry solution. Results from these experiments can also serve as a reference for comparison with solutions obtained with basic-state gradients. For both the dry and moist (uniform basic-state moisture) runs, the initial eddy energy, which includes both eddy potential and kinetic energy, decays at a rate of -0.02 day^{-1} and there are no significant differences between the dry and moist runs. In the absence of large-scale damping, hyperviscosity is responsible for this decay. Other dynamical variables, as well as precipitation in the moist run, show a similar decay with time. This indicates that interaction of a weak initial vortex with the release of latent heat alone is insufficient for growth, consistent with the cloud-system-resolving simulations of tropical depression spinup conducted by Murthy and Boos (2018).

a. Solutions with a basic-state moisture gradient

We now introduce a northward-increasing basic-state moisture field, systematically varying the gradient of the saturation profile (q_{sy}) and studying the influence of this basic-state property on the amplification of our initial weak, sinusoidal vorticity anomalies. We eliminate possible barotropic growth by setting the basic-state horizontal wind shear (ζ_s) to 0. The prescribed basic-state saturation column water vapor is of the form

$$q_s(\phi) = q_{s0} + \frac{q_{sy}}{2} \tanh\left(\frac{\phi - \phi_0}{\Delta\phi}\right), \tag{3}$$

where $\phi_0 = 20°$ and $\Delta\phi = 5°$. Here, q_{s0} sets the value of the basic-state q_s at 20°N and q_{sy} controls the meridional gradient of the background moist saturation field. A typical profile with $q_{s0} = 0.8$ m and a gradient of $q_{sy} = 0.2$ m (maximum change from equator to pole) is shown in Fig. 2a. This

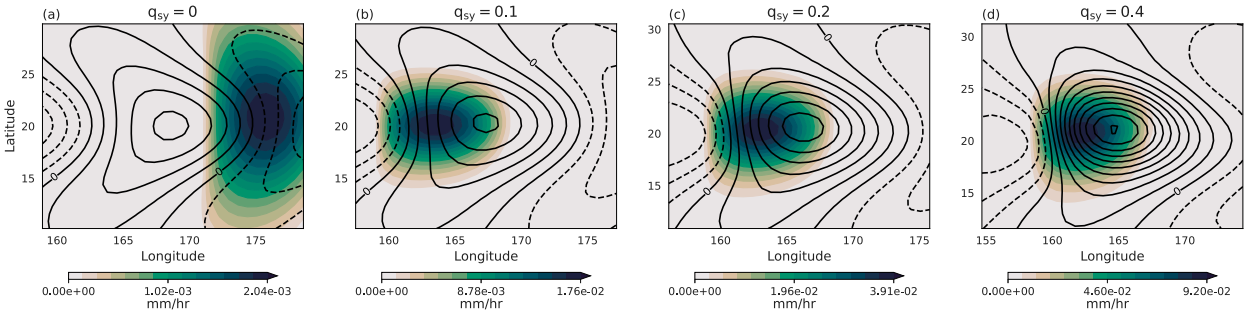

FIG. 3. Precipitation rate (colors) and vorticity (black contours with an interval of 2×10^{-8} s^{-1}) at day 3 for the experiments with varying basic-state moisture gradients (q_{sy}) and no wind shear ($\zeta_s = 0$). These are the responses to small-amplitude sinusoidal vorticity anomalies. The plot is centered at the maximum of one of the vortices. Precipitation occurs to the west of the vortex center except for the case with a zero moisture gradient, where it occurs to the east of the vortex center and is significantly weaker.

gradient value of 0.2 m is qualitatively similar to the fractional change in the observed water vapor mixing ratio (Diaz and Boos 2019b) and precipitable water (Chen et al. 2018) over South Asia, which varies meridionally by about 20%–30% (Fig. 1a). Further, for ease of comparison, all experiments use the same moist saturation value of $q_s = 0.8$ m at 20°N, with the basic-state moisture gradient (q_{sy}) varying from 0 (uniform moist case) to 0.4 m (with that maximum gradient setting q_s to 1 m on the poleward side of the gradient zone).

For the basic state with no moisture gradient, $q_{sy} = 0$, precipitation occurs to the east of the cyclonic vortex center (Fig. 3a). This is in contrast to the observations, where peak precipitation occurs to the west-southwest of the vortex center (Godbole 1977). In contrast, with a basic-state moisture gradient $q_{sy} = 0.2$ m, precipitation occurs to the west of the cyclonic vortex center and anomalies strengthen with time and propagate westward (Fig. 4). Eddy energy has a growth rate of 0.17 day^{-1}, close to the value of 0.23 day^{-1} obtained in the linear β-plane model used by Adames and Ming (2018a), which also imposed a meridional temperature gradient. As diabatic heating enhances positive vorticity anomalies, cyclones grow faster than anticyclones (Fig. 4).

The growth rates of vorticity, horizontal wind, and precipitation all increase with the basic-state moisture gradient (Figs. 3 and 5). The uniform saturation case ($q_{sy} = 0$) provides a useful contrast, as its precipitation occurs to the east of cyclonic vortices and its vorticity and precipitation decays with time, supporting the idea that a spatial structure in which peak precipitation lies west of peak vorticity is necessary for growth. The dynamical fields as well as the precipitation rate strengthens with increasing basic-state moisture gradient. The absolute precipitation rates in these simulations are not especially meaningful given the weak, quasi-linear nature of the disturbances and the fact that it is the product χP that couples with the dynamics. The sharp changes seen in the maximum meridional velocity around day 4 (Fig. 5a) is due to the maxima operator selecting different parts of the vortex, as time evolves.

We also assessed the sensitivity of our solutions to the zonal wavenumber and convective time scale. Broadly, our results agree with the solutions obtained by Adames and Ming (2018a), with strongest growth found around zonal wavenumber $k = 15$ and a convective time scale $\tau_c = 12$ h. As in Adames and Ming (2018a), we also find the precipitation shifts away from the vortex center with decreasing τ_c.

b. *Solutions with basic-state horizontal shear*

We now examine the evolution of the weak, sinusoidal vorticity anomalies in the presence of horizontal wind shear and a uniform moisture background ($q_{sy} = 0$). Based on the observed mean state of the South Asian monsoon (Fig. 1a), we construct a background wind shear using a vorticity strip,

$$\zeta(\phi) = \zeta_s \exp\left[-\left(\frac{\phi - \phi_0}{\Delta\phi}\right)^2\right], \tag{4}$$

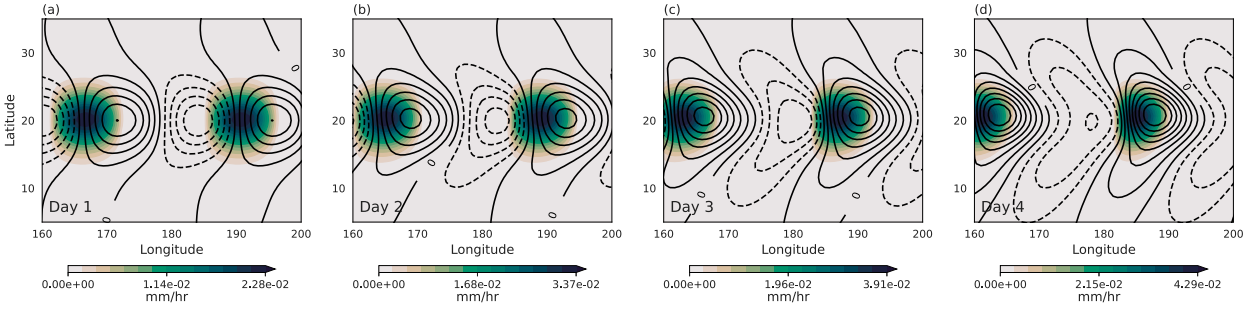

FIG. 4. The evolution of precipitation rate (colors) and vorticity (black contours with an interval of 2×10^{-8} s^{-1}) with time for the experiment with a basic-state moisture gradient $q_{sy} = 0.2$ m and no wind shear ($\zeta_s = 0$). The system is initially perturbed by small-amplitude sinusoidal vorticity anomalies centered at 20°N. The initial disturbance is strengthening with time and is propagating to the west.

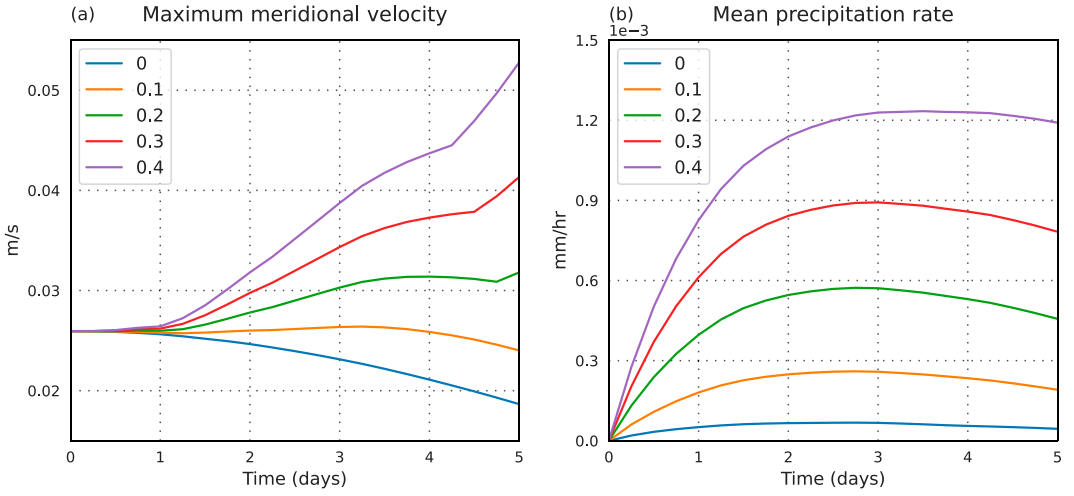

FIG. 5. Time series of the (a) maximum meridional velocity and (b) mean precipitation rate for the experiments with varying basic-state moisture gradients (q_{sy}) and no wind shear ($\zeta_s = 0$). These values are averaged over the entire domain and are the response to small-amplitude sinusoidal vorticity anomalies.

where $\phi_0 = 19°$ and $\Delta\phi = 3°$. The parameter ζ_s controls the magnitude of the basic-state shear and yields a zonal wind profile with a zero crossing at 20°N (Diaz and Boos 2019a, 2021a). Typical profiles of vorticity and the corresponding zonal wind for $\zeta_s = 4 \times 10^{-5}$ s^{-1} are shown in Figs. 2b and 2c.

Vorticity and precipitation at day 3 for various magnitudes of shear (ζ_s) are shown in Fig. 6. As we saw earlier, in the absence of a meridional moisture gradient, precipitation occurs east of cyclonic vortex centers and is an order of magnitude weaker than in the basic state having a moisture gradient but no shear (cf. magnitudes of precipitation between Figs. 5b and 7b). In the absence of a basic-state moisture gradient, precipitation is driven by convergence (which in this model serves as a proxy for the generation of convective instability by ascent) rather than the horizontal advection of moisture, which explains the weaker magnitude of precipitation and its position to the east of the cyclonic vortex in the region of convergence [see Fig. 3 in Kiladis et al. (2009) for similar structures in theoretical equatorial waves]. In contrast, horizontal wind anomalies are stronger for the basic state with shear than for the basic state with only a moisture gradient. With increasing shear, the initial sinusoidal fields become progressively distorted and precipitation becomes spatially decoupled from the vortex center. The circulation anomalies, as indicated by the meridional wind, grow stronger with shear, but the precipitation rate displays less sensitivity (Fig. 7; although precipitation increases greatly after day 3 for strong horizontal shears, this occurs far from the cyclonic vorticity centers and thus does not resemble the behavior of observed monsoon low pressure systems). The up-shear tilt of the perturbations and the absence of any other instability mechanisms suggest that the growth of the vorticity anomalies is due to barotropic instability (Peng et al. 2009). In essence, barotropic instability amplifies the circulation anomalies, but the growth rate of precipitation has less sensitivity to the shear in the absence of a moisture gradient.

c. *Solutions with a basic-state moisture gradient and horizontal shear*

We now examine solutions for basic states with both moisture gradients and horizontal shear, showing that the decoupling of precipitation from circulation anomalies, suggested in the

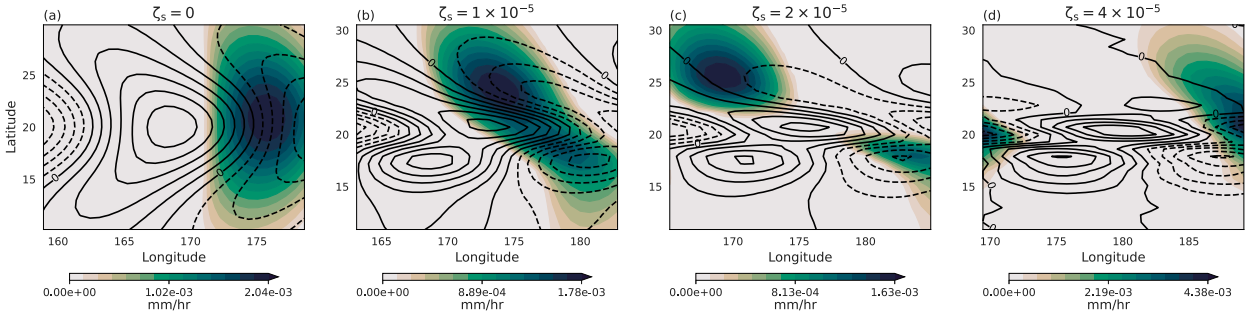

FIG. 6. Precipitation rate (colors) and vorticity (black contours with an interval of 5×10^{-8} s^{-1}) at day 3 for the experiments with varying wind shear (ζ_s) but with no basic-state moisture gradient ($q_{sy} = 0$). The system is initially perturbed by small-amplitude sinusoidal vorticity anomalies centered at 20°N. The vorticity contours are plotted after removing the imposed background shear. The domain is centered at the maxima of one of the vortices.

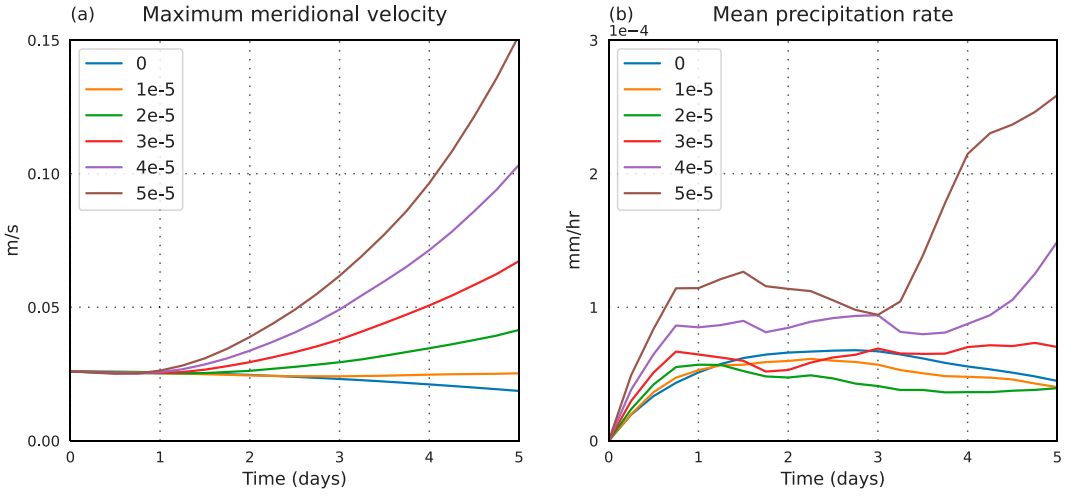

FIG. 7. Time series of the (a) maximum meridional velocity and (b) mean precipitation rate for the experiments with varying horizontal wind shear (ζ_s) but with no basic-state moisture gradient ($q_{sy} = 0$). These values are averaged over the entire domain and are the response to small-amplitude sinusoidal vorticity anomalies.

experiments described above, becomes even more evident when these basic-state gradients are combined. The time evolution of the maximum meridional velocity and mean precipitation rate for various moisture gradients with fixed horizontal shear is shown in Figs. 8a and 8b. While the meridional velocity increases with time (Fig. 8a), there is little sensitivity in the growth rate of meridional velocity to changes in the moisture gradient. The maximum meridional velocities achieved with this intermediate basic-state shear are roughly twice as large as those achieved with the strongest moisture gradient in the absence of horizontal shear (cf. with Fig. 5a), but the peak meridional velocities actually decrease slightly as the basic-state moisture gradient is increased. This suggests that the circulation anomalies are mostly driven by barotropic instability, and indeed their growth rate increases strongly with the basic-state shear (Fig. 8c). In contrast, precipitation is strongly affected by the moisture gradient (Fig. 8b), exhibiting little sensitivity to horizontal shear with a fixed moisture gradient (Fig. 8d; as in Fig. 7b, the increase in precipitation after day 3 occurs far from the cyclonic vorticity center and thus is a poor analog for observed monsoon depressions at that stage of the instability).

A summary of all the runs is presented in Figs. 9a–c, which show the amplification of the maximum meridional velocity and mean precipitation rate at day 3, relative to the moist run with no basic-state moisture gradient and no horizontal shear ($q_{sy} = 0$, $\zeta_s = 0$), together with the eddy energy growth rates averaged over days 2–4. The maximum meridional velocity and eddy energy growth depend strongly on the horizontal shear but only weakly on the moisture gradient, with an increase in the moisture gradient causing a modest increase in these dynamical measures for weak shear and a slight decrease for strong shear. In contrast, the mean precipitation rate is determined primarily by the moisture gradient.

4. Nonlinear isolated vortices

Now we consider a more realistic case, using the same basic states but where the initial perturbation takes the form of an isolated vortex strong enough to produce nonlinear effects. This vortex is intended to represent an idealized weak low pressure system that might intensify into a monsoon depression, and we examine how it evolves in basic states with different moisture gradients and horizontal wind shear. The initial vortex is generated using a height anomaly,

$$h'(\lambda,\phi) = h_{\text{pert}} \exp\left[-\left(\frac{\lambda-\lambda_0}{\Delta\lambda}\right)^2\right]\exp\left[-\left(\frac{\phi-\phi_0}{\Delta\phi}\right)^2\right], \qquad (5)$$

where $h_{\text{pert}} = -15$ m, λ is longitude, and the position and width parameters are $\lambda_0 = 180°$, $\phi_0 = 20°$, $\Delta\lambda = 5°$, and $\Delta\phi = 5°$. This yields an initial perturbation spanning a width of about 1000 km, with a balanced maximum meridional velocity of about 4.8 m s^{-1}, closely matching the peak rotational velocity in the initial anomaly imposed by Diaz and Boos (2021a).

The evolution of the initial vortex with a basic-state moisture gradient of $q_{sy} = 0.2$ m and a horizontal wind shear of $\zeta_s = 4 \times 10^{-5}$ s^{-1} is shown in Fig. 10. The initial vortex grows with time, both spatially and in magnitude.[1] For example, the maximum meridional velocity grows from its initial value of 4.8 m s^{-1} to about 8 m s^{-1} at the end of day 3. Similarly, precipitation intensifies and reaches its maximum around day 2. Although intense precipitation is also observed at later times, this occurs far east of the vortex center associated with remote secondary disturbances (Figs. 10c,d). Precipitation occurs to the

[1] Although the increase in vortex size will contribute to the growth rate of eddy energy, the fact that the spatial maximum of meridional wind also increases strongly shows that the vortex intensity is also amplifying. Though we do not decompose the eddy energy growth rate into components associated with changes in vortex size and vortex intensity, we note that the fractional changes in meridional wind amplitude can account for a large part of the exponential growth rate in eddy energy. For example, comparing Figs 9d and 9f, the peak eddy energy growth rate of 0.83 corresponds to an increase only slightly larger than the fractional increase of 2.08 seen in meridional wind ($e^{0.83} = 2.3$).

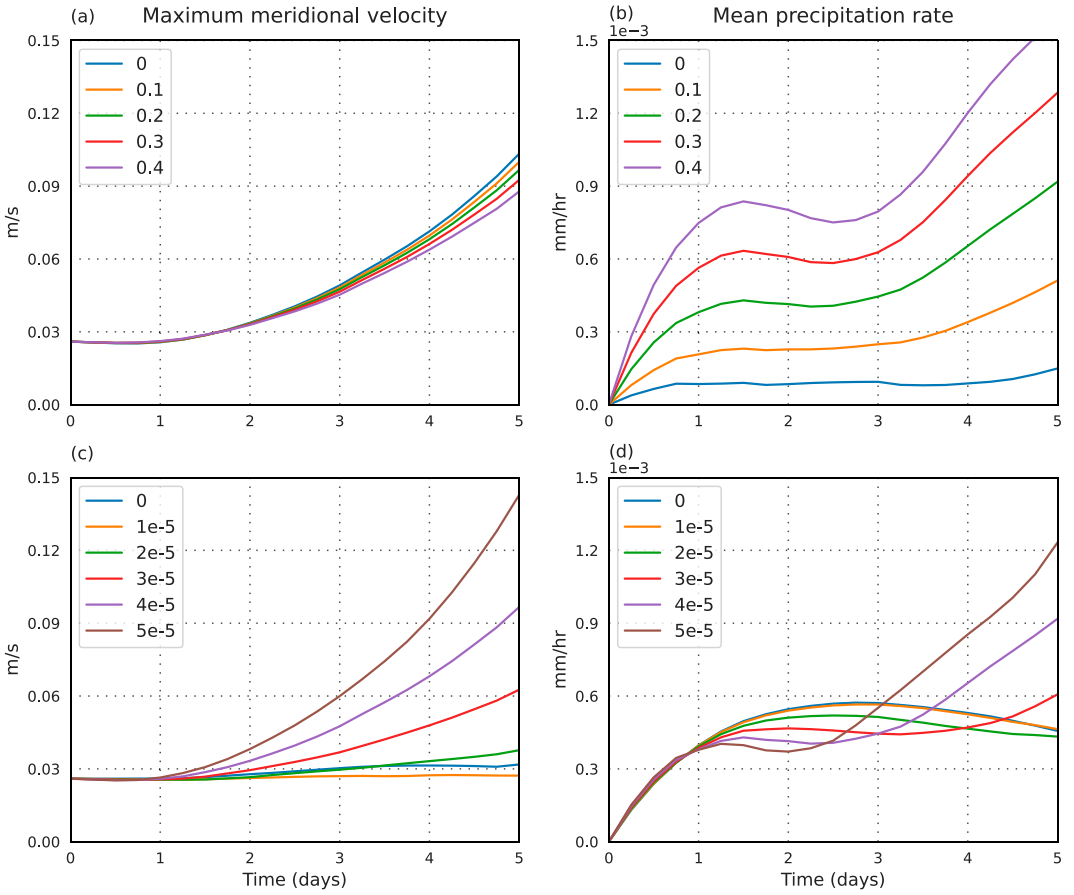

FIG. 8. Time series of the (a),(c) maximum meridional velocity and (b),(d) mean precipitation rate for the experiments with (a),(b) varying basic-state moisture gradient (q_{sy}) and a horizontal wind shear of $\zeta_s = 4 \times 10^{-5}$ s^{-1} and (c),(d) varying horizontal wind shear (ζ_s) with a basic-state moisture gradient of $q_{sy} = 0.2$ m. These values are averaged over the entire domain and are the response to small-amplitude sinusoidal vorticity anomalies.

west of the vortex center because, in the presence of a poleward basic-state moisture gradient, northerly winds produce advective moistening west of the cyclonic vortex. This peak precipitation lies in roughly the same location that experiences quasigeostrophic (QG) lifting due to background vertical shear, which has been argued to produce precipitation in observed monsoon depressions (e.g., Rao and Rajamani 1970). But in our shallow water model that QG lifting does not operate because there is no background vertical shear.

We show the time evolution of the maximum meridional velocity and mean precipitation rate for varying moisture gradient with fixed horizontal shear (Figs. 11a,b) and for a fixed moisture gradient with varying horizontal shear (Figs. 11c,d). In these time series, we isolate the evolution of a single vortex by selecting a limited domain (a 20° × 20° box) centered around the vorticity maximum, but we extend the zonal dimension by an additional 10° to the west for experiments with background moisture gradients and 10° to the east for experiments without those gradients. Although the size of this box exceeds the typical size of the observed LPS, we use this larger domain because the vortex in our idealized simulations grows beyond that typical size (Fig. 10). This is a limitation of these idealized model configurations, which we speculate may permit such spatial growth because their background horizontal shear and moisture gradients extend over all longitudes. However, Diaz and Boos (2019a) showed that the mechanism of barotropic growth that operated in a zonally infinite region of background shear was still relevant when that shear zone was zonally confined.

When the basic-state moisture gradient (q_{sy}) is increased while keeping the horizontal shear (ζ_s) fixed, the amplification rates of meridional velocity and mean precipitation rate both increase, but the intensification of the precipitation rate is stronger than that of meridional winds (Figs. 11a,b). Conversely, when horizontal shear is increased for a fixed basic-state moisture gradient, the amplification rate of meridional wind increases while the precipitation rates change little (Figs. 11c,d). In fact, the precipitation rate decreases by a small amount with increasing horizontal shear.

These results show that the isolated vortices exhibit similar sensitivities to basic-state properties as the small-amplitude sinusoidal modes. However, the sinusoidal modes continued to intensify past day 5, while the finite-amplitude vortex reaches its peak around days 3–4; while there are multiple possible

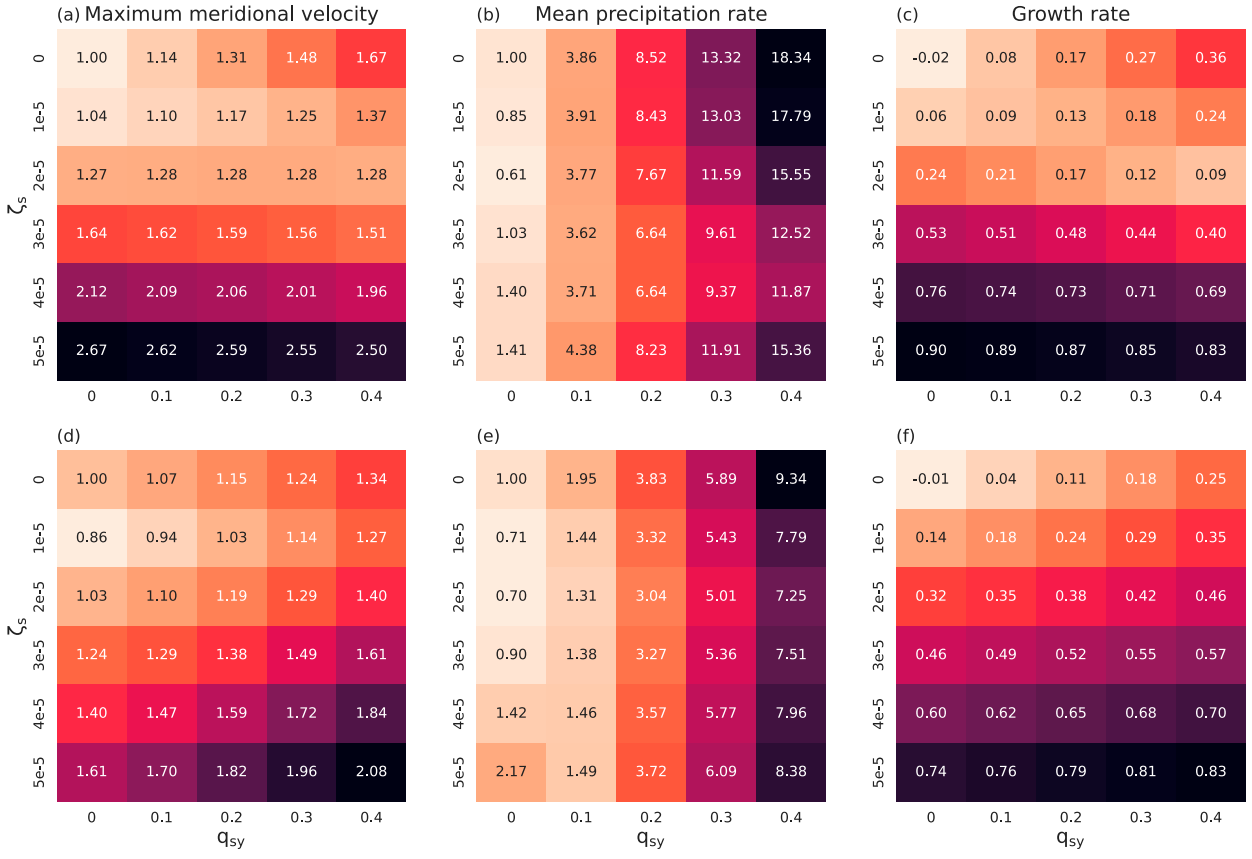

FIG. 9. Amplification of the (a),(d) spatial maximum of meridional velocity and (b),(e) spatial mean precipitation rate, and (c),(f) eddy energy growth rate, all as a function of varying basic-state moisture gradient (q_{sy}) and horizontal wind shear (ζ_s). Rows correspond to (a)–(c) runs with weak sinusoidal modes and in (d)–(f) runs with a finite-amplitude isolated vortex. The amplification of meridional velocity and precipitation rate is determined by taking the values at day 3 and normalizing by the corresponding values at day 3 for the moist run with no basic-state moisture gradient ($q_{sy} = 0$) and wind shear ($\zeta_s = 0$). Eddy energy includes both the eddy potential and kinetic energy, and the growth rates are averaged over days 2–4.

causes of this, such as a resonance of the sinusoidal modes, the simplest explanation seems to be that nonlinearities associated with the stronger initial perturbation limit, or saturate, the growth.[2] Furthermore, the growth of winds is more strongly affected by changes in the moisture gradient for the nonlinear, isolated vortex than for the quasi-linear sinusoidal modes. For example, the amplification of winds increases by a factor of about 1.5 when the basic-state moisture gradient is increased from $q_{sy} = 0$ to 0.2 m, similar to the idealized cloud-system-resolving simulations of Diaz and Boos (2021a); the shallow water model used here, however, permits testing of a wider range of q_{sy}. Nevertheless, when synthesizing results for all the experiments initialized with an isolated vortex, we see that the meridional velocity amplification and eddy growth rates are most sensitive to horizontal shear, while precipitation growth is set by the moisture gradient (Figs. 9d–f), similar to the sensitivities of the quasi-linear sinusoidal modes (Figs. 9a–c). Note that in these plots, as for the quasi-linear modes, the amplification of meridional velocity and precipitation rate are computed with respect to a moist run with no basic-state moisture gradient or horizontal shear ($q_{sy} = 0$ and $\zeta_s = 0$).

5. Phase relation between vorticity and precipitation

A pertinent question arises as to the mechanism of interaction between the two instability mechanisms. As discussed above, the growth of dynamic and convective fields seem to be somewhat decoupled, with the amplification of dynamical fields more strongly controlled by the horizontal shear, while precipitation growth is mostly determined by moisture gradients; this suggests interaction between the two instability mechanisms is weak. However, at stronger wind shears for the quasi-linear sinusoidal modes, the sensitivity of growth rates to the basic-state moisture gradient weakens and in some cases even hinders growth (Figs. 9a,c). A possible explanation is that the phase relation between vorticity and precipitation

[2] The growth extends beyond 5 days for sinusoidal perturbations with other wavenumbers, although we do not provide illustrations of the simulation output for those runs. We also see the growth having a peak within the first 5 days when a stronger initial sinusoidal perturbation is used.

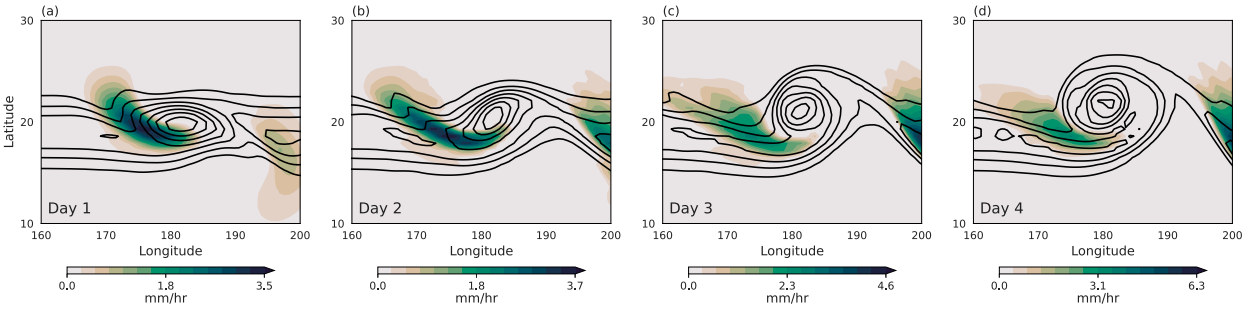

FIG. 10. The evolution of precipitation rate (colors) and vorticity (black contours with an interval of 1×10^{-5} s^{-1}) with time for the experiment with a basic-state moisture gradient $q_{sy} = 0.2$ m and wind shear $\zeta_s = 4 \times 10^{-5}$ s^{-1}. A finite-amplitude isolated vortex is used to initialize the model.

that favors growth becomes distorted in the presence of strong horizontal shear. Figure 12 shows the anomalous vorticity and precipitation at day 3, for runs with a basic-state moisture gradient of $q_{sy} = 0.2$ m and both types of initial disturbance. Two cases are shown, one without horizontal shear and the other with shear of $\zeta_s = 4 \times 10^{-5}$ s^{-1}. In the absence of shear, precipitation peaks to the west of the cyclonic vortex center (Figs. 12a,c), which in linear theory is

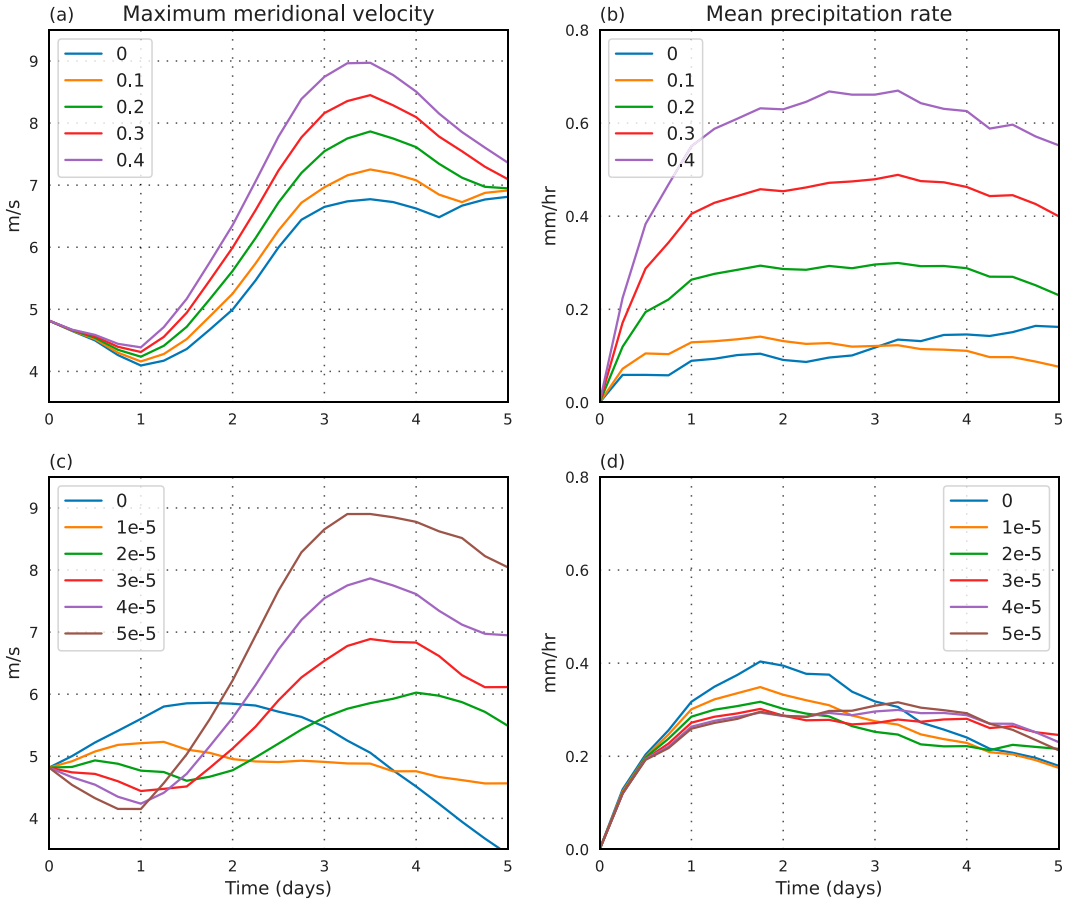

FIG. 11. Time series of the (a),(c) maximum meridional velocity and (b),(d) mean precipitation rate for the experiments with (a),(b) varying basic-state moisture gradient (q_{sy}) and a horizontal wind shear of $\zeta_s = 4 \times 10^{-5}$ s^{-1} and (c),(d) varying horizontal wind shear (ζ_s) with a basic-state moisture gradient of $q_{sy} = 0.2$ m. A finite-amplitude isolated vortex is used to initialize the model. We isolate the evolution of a single vortex by selecting a limited domain (a 20° × 20° box) centered around the vorticity maximum, but we extend the zonal dimension by an additional 10° to the west for experiments with background moisture gradients and 10° to the east for experiments without those gradients.

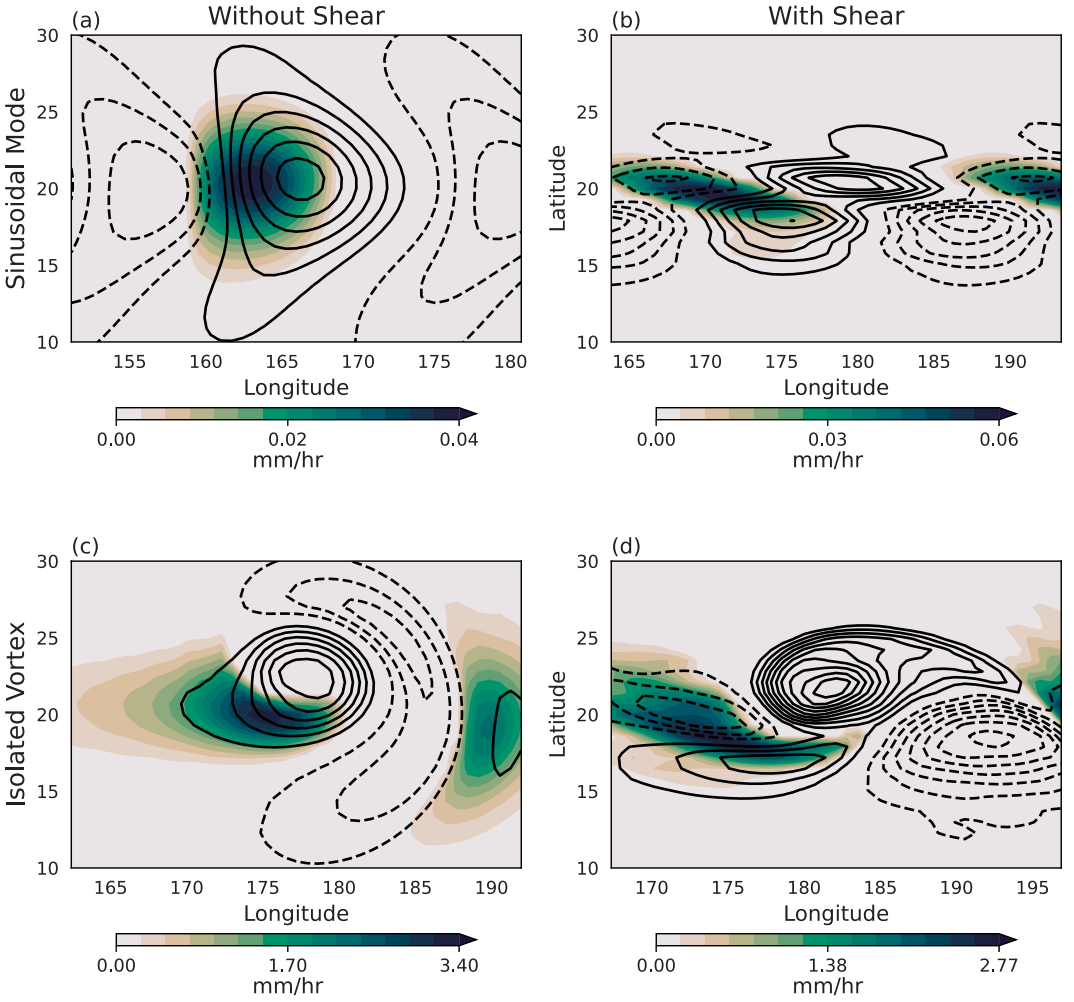

FIG. 12. Precipitation rate (colors) and vorticity (black contours) at day 3 for the experiments (a),(c) without wind shear and (b),(d) with a wind shear $\zeta_s = 4 \times 10^{-5}\ \mathrm{s}^{-1}$. All the plots have a basic-state moisture gradient of $q_{sy} = 0.2$ m. Rows correspond to (a),(b) runs with weak sinusoidal modes and (c),(d) runs with a finite-amplitude isolated vortex. The basic-state vorticity strip is removed from the vorticity fields before plotting. The vorticity contour interval is (a) 2×10^{-8}, (b) 5×10^{-8}, and (c),(d) $5 \times 10^{-6}\ \mathrm{s}^{-1}$.

argued to favor intensification (Adames and Ming 2018a). However, with strong horizontal shear, this phase relation is distorted and precipitation aligns more closely with an anticyclonic center (Figs. 12b,d). This structure resembles the damped mode in the linear theory of Adames and Ming (2018a). This effect seems to be stronger for the quasi-linear sinusoidal modes, but for nonlinear isolated vortices the sensitivities of the precipitation amplification rate and the eddy growth rate to the basic-state moisture gradient do decrease at higher horizontal shears (Figs. 9e,f). The spatial structure of vorticity that is associated with this distortion of the moist effects by strong horizontal shear bears some resemblance to observations; the zonally elongated vorticity anomaly to the southwest of the main cyclonic vortex center resembles that seen in a case study of a 2008 monsoon depression (Boos et al. 2017, their Figs. 9 and 10).

6. Summary and discussion

In this work, we aimed to understand the mechanism by which a monsoon depression–like vortex grows. With recent work noting the inconsistency of observed storm structures with the growth mechanism of baroclinic instability (Cohen and Boos 2016), we specifically examined the role played by two meridional gradients, in moisture and zonal wind shear, in their growth. Using a moist shallow water model in which we systematically varied these two gradients, we delineated the role played by moisture–vortex instability and barotropic growth in the intensification of initial disturbances.

To begin, we considered the growth of small-amplitude sinusoidal modes. In the absence of either a meridional moisture gradient or horizontal wind shear, that initial perturbation decayed with time, regardless of whether parameterized precipitation was included. This shows that at least one of the two

gradients is essential for growth in our shallow water model. When only a moisture gradient was introduced, disturbance growth occurred in a phenomenon originally referred to as a balanced tropical moisture wave (Sobel et al. 2001) and more recently termed moisture–vortex instability (Adames and Ming 2018a). With a poleward moisture gradient, the anomalies propagate westward with precipitation occurring to the west of the vorticity maxima. This leads to an enhancement of the vortex, with larger growth rates occurring as the basic-state moisture gradient was increased. The precipitation rates exhibited greater sensitivity than the vortex strength to changes in the moisture gradient. Overall, our low-amplitude (and thus quasi-linear) solutions in a spherical domain resembled the linear solutions obtained by Adames and Ming (2018a), with similar sensitivity to several model parameters. When meridional wind shear was instead imposed in the basic state, the intensification rate of horizontal winds increased with the shear but precipitation rates were weaker than in the presence of a moisture gradient and were comparatively insensitive to the shear. Also, in contrast to observations, precipitation occurred to the east of the vortex centers. In the presence of both a moisture gradient and wind shear in the basic state, the growth of dynamical fields was mainly controlled by the shear, while precipitation rates were mostly set by the moisture gradient.

A broadly similar picture emerged from our examination of the evolution of a finite-amplitude isolated vortex, with the growth of the dynamical fields being more sensitive to the horizontal shear than to the moisture gradient. However, the moisture gradient did affect the growth of dynamical fields to a greater extent than for the small-amplitude sinusoidal initial condition. Similar to the cloud-resolving simulation of Diaz and Boos (2021a), we saw an amplification of the winds by a factor of about 1.5 because of the inclusion of a moisture gradient in the basic state. The precipitation rate for the isolated vortex was mostly set by the moisture gradient, as in the quasi-linear sinusoidal modes. However, in contrast to those quasi-linear modes where the intensification occurred even after day 5, the vortex strength and precipitation rate peaked around days 3–4, suggesting the importance of nonlinear effects.

Acting alone, both barotropic and moisture–vortex instabilities lead to an intensification of an isolated vortex or a quasi-linear sinusoidal mode. But in combination their effects weaken slightly, as evidenced by a smaller sensitivity of growth rates to the basic-state gradients. Especially for strong wind shear, the contribution of moisture–vortex instability diminishes and in some cases even hinders disturbance growth. A possible explanation lies in the distortion of the phase relation between moisture anomalies and vorticity anomalies with increasing shear, which seems to disrupt the moisture–vortex instability. It is possible that interaction of the barotropic and moisture-vortex instabilities would change with different magnitudes and spatial structures of the background gradients. For example, for stronger background wind shears, the vortex amplification may be almost entirely due to barotropic growth if the background shears sufficiently distort the vortex's phase relation with moisture anomalies. The interaction of the two instabilities may also be influenced by the meridional width and zonal extent of the background gradients; indeed, the meridional shear associated with the observed monsoon trough over South Asia typically has a different meridional position and meridional width than the background moisture gradient (e.g., Fig. 1), as well as a somewhat different zonal extent. However, even in the absence of a true instability, moisture gradients may still alter precipitation by producing moisture advection or modifying the moisture content in regions experiencing dynamical lifting.

Even in the absence of any disruption of one instability mechanism by another, our results highlight the possibility that rotational winds in a lower-tropospheric vortex can intensify at different rates than the precipitating ascent in such a vortex. In other words, LPS need not have vertical and horizontal motion fields with fixed relative amplitudes; barotropic instability is a canonical example of a mechanism that primarily intensifies the rotational flow, and Diaz and Boos (2019b) argued that vertical motions might be generated in the presence of such barotropic growth primarily through dynamical coupling with a background vertical shear (e.g., via QG lifting). Our shallow water model does not include any representation of such vertical shear, so it is a framework in which the barotropic growth mechanism can be cleanly isolated from other diabatic mechanisms (such as moisture–vortex instability).

The presence of vertical shear and associated QG lifting has long been thought to influence precipitation in monsoon depressions (Rao and Rajamani 1970; Sanders 1984), with the location of peak precipitation well predicted by solutions of the adiabatic QG omega equation (Boos et al. 2015). The dynamical lifting produced by the interaction of the vortex with the background vertical shear has been argued to be amplified by a feedback with moist convection, thereby enhancing monsoon depression precipitation (Nie and Sobel 2016; Murthy and Boos 2020). However, in our single-layer shallow water model, vertical shear is not included and the effect of QG lifting is ignored, which is a limitation of this study. It is unclear whether this is a major deficiency, because in the idealized cloud-system-resolving simulations of Diaz and Boos (2021a), vertical shear was found to be important in monsoon depression amplification primarily through its effect on the meridional moisture gradient (their basic state used constant relative humidity, so any vertical shear was accompanied by a moisture gradient, through thermal wind balance). That effect is represented in our shallow water model by the prescription of an initial moisture gradient and a saturation moisture gradient. Whether QG lifting due to vertical shear is additionally important for amplification merits further exploration.

The result that both meridional moisture gradients and meridional wind shear may be vital for the growth of monsoon depressions was suggested by Diaz and Boos (2021a), but the convection-permitting simulations used in that study did not allow the wide exploration of parameter space undertaken here. Furthermore, the existence of differing sensitivities of the vortex intensification rate and the precipitation intensification rate to these two environmental gradients is a novel finding. Further work needs to be done to determine whether these results are affected by QG uplift due to coupling with background vertical shear, stratification, or other effects that cannot be represented in a two-dimensional shallow water model.

In addition to further modeling for the goal of understanding mechanisms, a useful next step might be to examine the consistency of the mechanisms described here with the observed amplification of monsoon depressions. Other future work might explore the implications of these results for forecasts of monsoon LPS. For example, the dry bias in low-level relative humidity seen in a high-resolution numerical model used for weather forecasting over India (Mukhopadhyay et al. 2019) may explain why that model has biases in its representation of the intensification of monsoon LPS (Sarkar et al. 2021). These issues have great importance for disaster preparedness, given the large fraction of South Asian hydrological disasters that are associated with monsoon LPS (Suhas et al. 2022).

Acknowledgments. The authors acknowledge financial support from the Earth System Science Organization, Ministry of Earth Sciences, Government of India (Grant IITM/MM-II/Univ_California_USA/INT-3) to conduct this research under the Monsoon Mission. The authors also acknowledge support from the U.S. Department of Energy, Office of Science, Office of Biological and Environmental Research, Climate and Environmental Sciences Division, Regional and Global Model Analysis Program, under Award DE-SC0019367. This work used resources of the National Energy Research Scientific Computing Center (NERSC), which is a DOE Office of Science User Facility.

Data availability statement. The moist shallow water code used to run the simulations is available on GitHub (https://github.com/suhasdl/pySWE). ERA5 data were downloaded from the Copernicus Climate Change Service Climate Data Store (CDS) website (https://cds.climate.copernicus.eu). Numerical simulation data are available from the authors upon request.

REFERENCES

Adames, Á. F., 2021: Interactions between water vapor, potential vorticity, and vertical wind shear in quasi-geostrophic motions: Implications for rotational tropical motion systems. *J. Atmos. Sci.*, **78**, 903–923, https://doi.org/10.1175/JAS-D-20-0205.1.

——, and Y. Ming, 2018a: Interactions between water vapor and potential vorticity in synoptic-scale monsoonal disturbances: Moisture vortex instability. *J. Atmos. Sci.*, **75**, 2083–2106, https://doi.org/10.1175/JAS-D-17-0310.1.

——, and ——, 2018b: Moisture and moist static energy budgets of South Asian monsoon low pressure systems in GFDL AM4.0. *J. Atmos. Sci.*, **75**, 2107–2123, https://doi.org/10.1175/JAS-D-17-0309.1.

Ajayamohan, R. S., W. J. Merryfield, and V. V. Kharin, 2010: Increasing trend of synoptic activity and its relationship with extreme rain events over central India. *J. Climate*, **23**, 1004–1013, https://doi.org/10.1175/2009JCLI2918.1.

Bembenek, E., T. M. Merlis, and D. N. Straub, 2021: Influence of latitude and moisture effects on the barotropic instability of an idealized ITCZ. *J. Atmos. Sci.*, **78**, 2677–2689, https://doi.org/10.1175/JAS-D-20-0346.1.

Betts, A. K., 1986: A new convective adjustment scheme. Part I: Observational and theoretical basis. *Quart. J. Roy. Meteor. Soc.*, **112**, 677–691, https://doi.org/10.1002/qj.49711247307.

Boos, W. R., J. V. Hurley, and V. S. Murthy, 2015: Adiabatic westward drift of Indian monsoon depressions. *Quart. J. Roy. Meteor. Soc.*, **141**, 1035–1048, https://doi.org/10.1002/qj.2454.

——, B. E. Mapes, and V. S. Murthy, 2017: Potential vorticity structure and propagation mechanism of Indian monsoon depressions. *The Global Monsoon System: Research and Forecast*, World Scientific, 187–199.

Bouchut, F., J. Lambaerts, G. Lapeyre, and V. Zeitlin, 2009: Fronts and nonlinear waves in a simplified shallow-water model of the atmosphere with moisture and convection. *Phys. Fluids*, **21**, 116604, https://doi.org/10.1063/1.3265970.

Chen, X., O. M. Pauluis, L. R. Leung, and F. Zhang, 2018: Multiscale atmospheric overturning of the Indian summer monsoon as seen through isentropic analysis. *J. Atmos. Sci.*, **75**, 3011–3030, https://doi.org/10.1175/JAS-D-18-0068.1.

Clark, S. K., Y. Ming, and Á. F. Adames, 2020: Monsoon low pressure system–like variability in an idealized moist model. *J. Climate*, **33**, 2051–2074, https://doi.org/10.1175/JCLI-D-19-0289.1.

Cohen, N. Y., and W. R. Boos, 2016: Perspectives on moist baroclinic instability: Implications for the growth of monsoon depressions. *J. Atmos. Sci.*, **73**, 1767–1788, https://doi.org/10.1175/JAS-D-15-0254.1.

Diaz, M., and W. R. Boos, 2019a: Barotropic growth of monsoon depressions. *Quart. J. Roy. Meteor. Soc.*, **145**, 824–844, https://doi.org/10.1002/qj.3467.

——, and ——, 2019b: Monsoon depression amplification by moist barotropic instability in a vertically sheared environment. *Quart. J. Roy. Meteor. Soc.*, **145**, 2666–2684, https://doi.org/10.1002/qj.3585.

——, and ——, 2021a: Evolution of idealized vortices in monsoon-like shears: Application to monsoon depressions. *J. Atmos. Sci.*, **78**, 1207–1225, https://doi.org/10.1175/JAS-D-20-0286.1.

——, and ——, 2021b: The influence of surface heat fluxes on the growth of idealized monsoon depressions. *J. Atmos. Sci.*, **78**, 2013–2027, https://doi.org/10.1175/JAS-D-20-0359.1.

Fletcher, J. K., D. J. Parker, K. M. R. Hunt, G. Vishwanathan, and M. Govindankutty, 2018: The interaction of Indian monsoon depressions with northwesterly midlevel dry intrusions. *Mon. Wea. Rev.*, **146**, 679–693, https://doi.org/10.1175/MWR-D-17-0188.1.

Frierson, D. M. W., A. J. Majda, and O. M. Pauluis, 2004: Large scale dynamics of precipitation fronts in the tropical atmosphere: A novel relaxation limit. *Commun. Math. Sci.*, **2**, 591–626, https://doi.org/10.4310/CMS.2004.v2.n4.a3.

Galewsky, J., R. K. Scott, and L. M. Polvani, 2004: An initial-value problem for testing numerical models of the global shallow-water equations. *Tellus*, **56A**, 429–440, https://doi.org/10.3402/tellusa.v56i5.14436.

Gill, A. E., 1982: Studies of moisture effects in simple atmospheric models: The stable case. *Geophys. Astrophys. Fluid Dyn.*, **19**, 119–152, https://doi.org/10.1080/03091928208208950.

Godbole, R. V., 1977: The composite structure of the monsoon depression. *Tellus*, **29A**, 25–40, https://doi.org/10.3402/tellusa.v29i1.11327.

Goswami, B. N., R. N. Keshavamurty, and V. Satyan, 1980: Role of barotropic, baroclinic and combined barotropic-baroclinic instability for the growth of monsoon depressions and mid-

tropospheric cyclones. *Proc. Indian Acad. Sci.*, **89**, 79–97, https://doi.org/10.1007/BF02841521.

Hunt, K. M. R., and J. K. Fletcher, 2019: The relationship between Indian monsoon rainfall and low-pressure systems. *Climate Dyn.*, **53**, 1859–1871, https://doi.org/10.1007/s00382-019-04744-x.

Hurley, J. V., and W. R. Boos, 2015: A global climatology of monsoon low-pressure systems. *Quart. J. Roy. Meteor. Soc.*, **141**, 1049–1064, https://doi.org/10.1002/qj.2447.

Keshavamurty, R. N., 1972: On the vertical tilt of monsoon disturbances. *J. Atmos. Sci.*, **29**, 993–995, https://doi.org/10.1175/1520-0469(1972)029<0993:OTVTOM>2.0.CO;2.

Kiladis, G. N., M. C. Wheeler, P. T. Haertel, K. H. Straub, and P. E. Roundy, 2009: Convectively coupled equatorial waves. *Rev. Geophys.*, **47**, RG2003, https://doi.org/10.1029/2008RG000266.

Kraucunas, I., and D. L. Hartmann, 2007: Tropical stationary waves in a nonlinear shallow-water model with realistic basic states. *J. Atmos. Sci.*, **64**, 2540–2557, https://doi.org/10.1175/JAS3920.1.

Krishnakumar, V., R. N. Keshavamurty, and S. V. Kasture, 1992: Moist baroclinic instability and the growth of monsoon depressions—Linear and nonlinear studies. *Proc. Indian Acad. Sci.*, **101**, 123–152, https://doi.org/10.1007/BF02840349.

Krishnamurti, T. N., M. Kanamitsu, R. Godbole, C.-B. Chang, F. Carr, and J. H. Chow, 1976: Study of a monsoon depression (II), dynamical structure. *J. Meteor. Soc. Japan*, **54**, 208–225, https://doi.org/10.2151/jmsj1965.54.4_208.

——, A. Martin, R. Krishnamurti, A. Simon, A. Thomas, and V. Kumar, 2013: Impacts of enhanced CCN on the organization of convection and recent reduced counts of monsoon depressions. *Climate Dyn.*, **41**, 117–134, https://doi.org/10.1007/s00382-012-1638-z.

Lambaerts, J., G. Lapeyre, and V. Zeitlin, 2011: Moist versus dry barotropic instability in a shallow-water model of the atmosphere with moist convection. *J. Atmos. Sci.*, **68**, 1234–1252, https://doi.org/10.1175/2011JAS3540.1.

——, ——, and ——, 2012: Moist versus dry baroclinic instability in a simplified two-layer atmospheric model with condensation and latent heat release. *J. Atmos. Sci.*, **69**, 1405–1426, https://doi.org/10.1175/JAS-D-11-0205.1.

Lindzen, R. S., B. Farrell, and A. J. Rosenthal, 1983: Absolute barotropic instability and monsoon depressions. *J. Atmos. Sci.*, **40**, 1178–1184, https://doi.org/10.1175/1520-0469(1983)040<1178:ABIAMD>2.0.CO;2.

Mishra, S. K., and P. S. Salvekar, 1980: Role of baroclinic instability in the development of monsoon disturbances. *J. Atmos. Sci.*, **37**, 383–394, https://doi.org/10.1175/1520-0469(1980)037<0383:ROBIIT>2.0.CO;2.

Monteiro, J. M., Á. F. Adames, J. M. Wallace, and J. S. Sukhatme, 2014: Interpreting the upper level structure of the Madden-Julian oscillation. *Geophys. Res. Lett.*, **41**, 9158–9165, https://doi.org/10.1002/2014GL062518.

Moorthi, S., and A. Arakawa, 1985: Baroclinic instability with cumulus heating. *J. Atmos. Sci.*, **42**, 2007–2031, https://doi.org/10.1175/1520-0469(1985)042<2007:BIWCH>2.0.CO;2.

Mukhopadhyay, P., and Coauthors, 2019: Performance of a very high-resolution Global Forecast System model (GFS T1534) at 12.5 km over the Indian region during the 2016–2017 monsoon seasons. *J. Earth Syst. Sci.*, **128**, 155, https://doi.org/10.1007/s12040-019-1186-6.

Muller, C. J., L. E. Back, P. A. O'Gorman, and K. A. Emanuel, 2009: A model for the relationship between tropical precipitation and column water vapor. *Geophys. Res. Lett.*, **36**, L16804, https://doi.org/10.1029/2009GL039667.

Murthy, V. S., and W. R. Boos, 2018: Role of surface enthalpy fluxes in idealized simulations of tropical depression spinup. *J. Atmos. Sci.*, **75**, 1811–1831, https://doi.org/10.1175/JAS-D-17-0119.1.

——, and ——, 2020: Quasigeostrophic controls on precipitating ascent in monsoon depressions. *J. Atmos. Sci.*, **77**, 1213–1232, https://doi.org/10.1175/JAS-D-19-0202.1.

Nie, J., and A. H. Sobel, 2016: Modeling the interaction between quasigeostrophic vertical motion and convection in a single column. *J. Atmos. Sci.*, **73**, 1101–1117, https://doi.org/10.1175/JAS-D-15-0205.1.

Nitta, T., and K. Masuda, 1981: Observational study of a monsoon depression developed over the Bay of Bengal during summer MONEX. *J. Meteor. Soc. Japan*, **59**, 672–682, https://doi.org/10.2151/jmsj1965.59.5_672.

Paldor, N., O. Shamir, and C. I. Garfinkel, 2021: Barotropic instability of a zonal jet on the sphere: From non-divergence through quasi-geostrophy to shallow water. *Geophys. Astrophys. Fluid Dyn.*, **115**, 15–34, https://doi.org/10.1080/03091929.2020.1724996.

Peng, J., T. Li, M. S. Peng, and X. Ge, 2009: Barotropic instability in the tropical cyclone outer region. *Quart. J. Roy. Meteor. Soc.*, **135**, 851–864, https://doi.org/10.1002/qj.408.

Rajamani, S., and D. N. Sikdar, 1989: Some dynamical characteristics and thermal structure of monsoon depressions over the Bay of Bengal. *Tellus*, **41A**, 255–269, https://doi.org/10.3402/tellusa.v41i3.11838.

Rao, K. V., and S. Rajamani, 1970: Diagnostic study of a monsoon depression by geostrophic baroclinic model. *Mausam*, **21**, 187–194, https://doi.org/10.54302/mausam.v21i2.5366.

Rostami, M., and V. Zeitlin, 2017: Influence of condensation and latent heat release upon barotropic and baroclinic instabilities of vortices in a rotating shallow water *f*-plane model. *Geophys. Astrophys. Fluid Dyn.*, **111**, 1–31, https://doi.org/10.1080/03091929.2016.1269897.

——, and ——, 2019a: Eastward-moving convection-enhanced modons in shallow water in the equatorial tangent plane. *Phys. Fluids*, **31**, 021701, https://doi.org/10.1063/1.5080415.

——, and ——, 2019b: Geostrophic adjustment on the equatorial beta-plane revisited. *Phys. Fluids*, **31**, 081702, https://doi.org/10.1063/1.5110441.

Rydbeck, A. V., and E. D. Maloney, 2014: Energetics of east Pacific easterly waves during intraseasonal events. *J. Climate*, **27**, 7603–7621, https://doi.org/10.1175/JCLI-D-14-00211.1.

Saha, K., and C.-P. Chang, 1983: The baroclinic processes of monsoon depressions. *Mon. Wea. Rev.*, **111**, 1506–1514, https://doi.org/10.1175/1520-0493(1983)111<1506:TBPOMD>2.0.CO;2.

Salvekar, P. S., L. George, and S. K. Mishra, 1986: Low level wind shear and baroclinic growth of monsoon depression scale waves. *Meteor. Atmos. Phys.*, **35**, 10–18, https://doi.org/10.1007/BF01029520.

Sanders, F., 1984: Quasi-geostrophic diagnosis of the monsoon depression of 5–8 July 1979. *J. Atmos. Sci.*, **41**, 538–552, https://doi.org/10.1175/1520-0469(1984)041<0538:QGDOTM>2.0.CO;2.

Sarkar, S., P. Mukhopadhyay, S. Dutta, R. Phani Murali Krishna, R. D. Kanase, V. Prasad, and M. S. Deshpande, 2021: GFS model fidelity in capturing the transition of low-pressure area to monsoon depression. *Quart. J. Roy. Meteor. Soc.*, **147**, 2625–2637, https://doi.org/10.1002/qj.4024.

Schaeffer, N., 2013: Efficient spherical harmonic transforms aimed at pseudospectral numerical simulations. *Geochem. Geophys. Geosyst.*, **14**, 751–758, https://doi.org/10.1002/ggge.20071.

Shukla, J., 1977: Barotropic-baroclinic instability of mean zonal wind during summer monsoon. *Pure Appl. Geophys.*, **115**, 1449–1461, https://doi.org/10.1007/BF00874418.

Sikka, D. R., 1978: Some aspects of the life history, structure and movement of monsoon depressions. *Monsoon Dynamics*, Springer, 1501–1529.

Sobel, A. H., J. Nilsson, and L. M. Polvani, 2001: The weak temperature gradient approximation and balanced tropical moisture waves. *J. Atmos. Sci.*, **58**, 3650–3665, https://doi.org/10.1175/1520-0469(2001)058<3650:TWTGAA>2.0.CO;2.

Subrahmanyam, D., M. K. Tandon, L. George, and S. K. Mishra, 1981: Role of barotropic mechanism in the development of a monsoon depression: A MONEX study. *Pure Appl. Geophys.*, **119**, 901–912, https://doi.org/10.1007/BF00878958.

Suhas, D. L., and J. Sukhatme, 2020: Moist shallow-water response to tropical forcing: Initial-value problems. *Quart. J. Roy. Meteor. Soc.*, **146**, 3695–3714, https://doi.org/10.1002/qj.3867.

——, N. Ramesh, R. M. Kripa, and W. R. Boos, 2022: Influence of monsoon low pressure systems on South Asian disasters and implications for disaster prediction. Research Square, https://doi.org/10.21203/rs.3.rs-1498790/v1.

Wheeler, M., G. N. Kiladis, and P. J. Webster, 2000: Large-scale dynamical fields associated with convectively coupled equatorial waves. *J. Atmos. Sci.*, **57**, 613–640, https://doi.org/10.1175/1520-0469(2000)057<0613:LSDFAW>2.0.CO;2.

Zeitlin, V., 2018: *Geophysical Fluid Dynamics: Understanding (Almost) Everything with Rotating Shallow Water Models*. Oxford University Press, 488 pp.